Available online at www.sciencedirect.com
SCIENCE DIRECT®
Journal of Solid State Chemistry 179 (2006) 512–521
JOURNAL OF SOLID STATE CHEMISTRY
www.elsevier.com/locate/jssc

Neutron diffraction and MAS NMR of Cesium Tungstate defect pyrochlores

K.R. Whittle*, G.R. Lumpkin, S.E. Ashbrook

Department of Earth Sciences, Cambridge Centre for Ceramic Immobilisation (C^3i), University of Cambridge, Downing Street, Cambridge CB2 3EQ, UK

Received 7 June 2005; received in revised form 2 November 2005; accepted 6 November 2005
Available online 15 December 2005

Abstract

Defect-pyrochlores based on the formulation $CsM_{0.5}W_{1.5}O_6$ (M = Ti, Ti/Zr, Zr and Hf) have been studied using neutron diffraction and magic-angle spinning nuclear magnetic resonance (MAS NMR). The results show that structural changes are linearly linked to the change in ionic-radius for the B-site, e.g. the unit cell changes from 10.2763 Å for $CsTi_{0.5}W_{1.5}O_6$ to 10.3820 Å for $CsZr_{0.4}W_{1.6}O_6$. Changes in the NMR chemical shift correlate with the change in electronegativity on the B-site, and show the presence of only one Cs crystal site.

Keywords: Defect pyrochlore; 133Cs MAS NMR

1. Introduction

Materials with the crystal structure of pyrochlore, general formulation $A_2B_2O_6Y$, have been found to contain a wide variety of metal cations on both the A- and B-sites, e.g. Ca, Na, and Ln on the A-site, with Nb, Ta and Ti on the B-site. Such materials have widespread uses in ionic conductivity [1], ferromagnetism [2], and chemical immobilisation of environmentally unfriendly waste [3].

The classical pyrochlore structure type [4,5], $A_2B_2O_6Y$, where in most cases $Y = O$, is a superstructure of the fluorite (MX_2) structure, and based upon a $2 \times 2 \times 2$ supercell containing M_4O_8, with ordered vacancies in the oxide anionic lattice. The symmetry of pyrochlore is $Fd\bar{3}m$, while that of fluorite is $Fm\bar{3}m$. The cation superstructure is based upon ordering of A cations parallel to the $\langle 110 \rangle$ direction, with the B cations also parallel to the $\langle 110 \rangle$ direction but shifted by $(\frac{1}{2}, \frac{1}{2}, \frac{1}{2})$, with respect to the origin. Using Wyckoff notation these are located on the 16c (0,0,0) and 16d $(\frac{1}{2}, \frac{1}{2}, \frac{1}{2})$ atomic positions. The local oxygen coordination of A is that of an axially distorted cube, while B is octahedral. A diagrammatic representation comparing classical pyrochlore with fluorite, and defect pyrochlores, is shown in Fig. 1.

Since the total cationic charge in these systems is normally +14, and the ideal fluorite formulation would give rise to a total anionic charge of −16, there are vacancies within the oxygen array. In pyrochlore they are located on specific positions in the lattice, and their location, in a perfect system, can be predicted from knowing the charges on the A- and B-sites. There are three crystallographically distinct sites in the pyrochlore lattice which O can occupy, these are the 48f $(x, \frac{1}{8}, \frac{1}{8})$, 8$a$ $(\frac{1}{8}, \frac{1}{8}, \frac{1}{8})$, which have local symmetries of *mm* and *43m*, respectively, and 8b $(\frac{3}{8}, \frac{3}{8}, \frac{3}{8})$, local symmetry *43m*, which is vacant in these systems. This vacancy allows the adjacent O^{2-} anions to relax into the void as there is no repulsion/blockage, which results in the value of the x coordinate of the oxygen atom on the 48f site changing from 0.375 in the ideal fluorite structure to 0.419 in $La_2Zr_2O_7$. A value of 0.4375 has been reported as the limit in classical pyrochlores based upon the summation of two oxide/fluoride radii [4]. There are many reviews of the properties of the classical pyrochlore structure available in the literature [4,5].

If the composition of the pyrochlore is changed from $A_2B_2O_7$ (e.g. $La_2Zr_2O_7$), to AB_2O_6 ($CsTi_{0.5}W_{1.5}O_6$), then a

*Corresponding author. Fax: +44 1223 333 450.
E-mail address: kwhi02@esc.cam.ac.uk (K.R. Whittle).

0022-4596/$ - see front matter © 2005 Elsevier Inc. All rights reserved.
doi:10.1016/j.jssc.2005.11.011

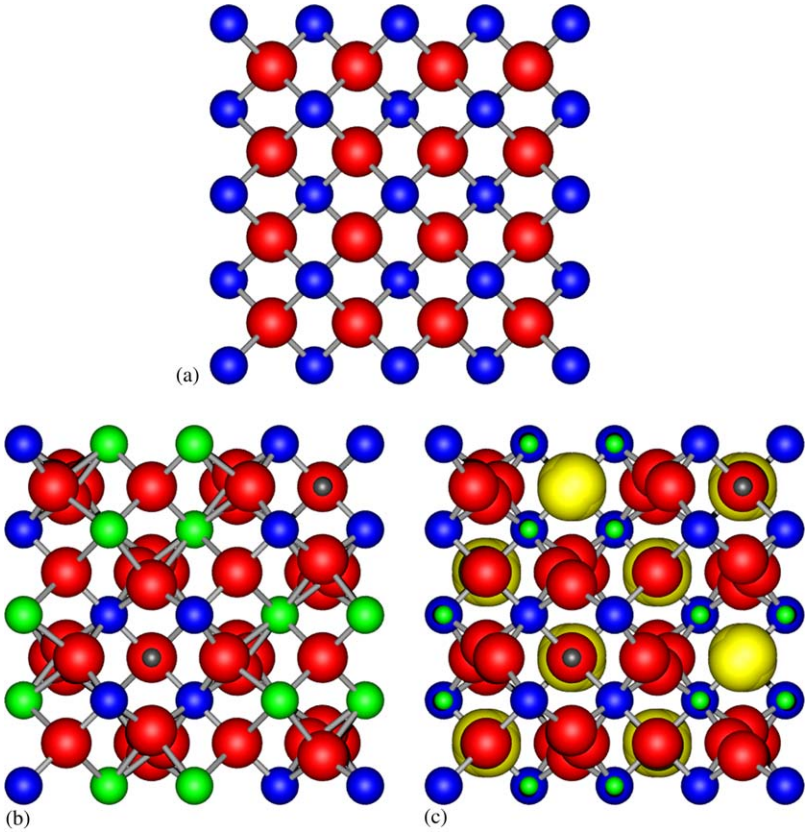

Fig. 1. Example projections along the [110] direction of (a) fluorite, (b) classical pyrochlore, and (c) Cs-containing pyrochlore. In (a) the red spheres are the oxygen and the blue spheres the cations. In (b) and (c) the red spheres are oxygen and the small black spheres are the unoccupied 8*b* position, the blue spheres are the *B*-site and the green spheres are the *A*-site. In (c) the Cs cation located on the 32*e* position is shown in yellow. In all images small spheres indicate the position of an unoccupied site.

structural modification arises. As the composition in the example system reduces the overall cation charge from +14 to +12, the charge balance is maintained by the removal of the *Y*-site anion, which has further implications for the arrangement of the cations. As the systems studied here contains Cs^+, a large cation ~1.5–1.8 Å [6,7], the classical location on the 16*c* site is no longer easily possible, thus a new location within the unit-cell is often adopted by large monovalent and divalent cations.

In the early papers on these types of pyrochlore it was thought that the *A* cation was located on the 8*a* position, primarily due to the X-ray diffraction facilities available at the time. Subsequently, the position of the *A* cation has been modified to now be the special 32*e* position, (*x*,*x*,*x*), which is located between the 8*a* and 16*c* sites. Due to the nature of the 32*e* position, and the size of the cations, it is not possible to have a full occupancy; only an $\frac{1}{4}$ occupancy is possible which can result in the appearance of the position being identical to that of 8*a*, especially when the position is close to $(\frac{1}{8},\frac{1}{8},\frac{1}{8})$. This new position of 32*e* has implications for the classical 48*f* position, as the previous traditional limit of 0.4375 is no longer valid. Primarily this is due to the large cationic size of the Cs^+ and the relatively small *B*-site cation, which is always bonded to the 48*f* site, thus the value for the 48*f* position can be larger then 0.4375.

Previous work on these types of pyrochlore have tended to examine their properties as ionic conductors [8]. In this work the primary motivation was to accurately determine the structure of four Cs-pyrochlores, containing Ti, Ti/Zr, Hf and Zr. There were two reasons behind this; firstly, in examining the effect of radiation damage it is not easy to determine the effect of composition on stability whilst eliminating as much structural change as possible. In pyrochlores this is particularly apparent as Ti and Zr/Hf have differing stability fields. The stability range of compositions by which pyrochlore is the stable phase lie within the radius ratio [5] of *A*- and *B*-site cations (R_A and R_B) between 1.78 and 1.42, e.g. $Gd_2Ti_2O_7$ is near the beginning of the Ti stability field (R_A/R_B~1.74), while $Gd_2Zr_2O_7$ is at the end of the Zr stability field (R_A/R_B~1.48). Radius ratios that lie below this value tend to form a defect-fluorite phase, while those higher form a monoclinic structure. In the systems studied here it is possible to study the effect of composition on structurally identical materials. The structural effect of radiation damage on pyrochlore is of particular importance as the structure type is frequently suggested as a wasteform for radioactive nuclear waste [9]. During the radioactive decay of a large number of elements results in damage to the structure, in some cases transforming to a defect-fluorite

while in others it becomes amorphous. The degree of stability to radiation damage is often affected by the composition of the elements e.g. $Gd_2Ti_2O_7$ becomes amorphous while $Gd_2Zr_2O_7$ transforms to a defect-fluorite. We are presently using ion-beam irradiation for the study of radiation damage; the results being obtained will be the subject of a further publication. In order to investigate the radiation stability of such materials, whether experimentally or computationally requires accurate structural information on the samples being studied.

A supplementary motivation was to apply the techniques of neutron powder diffraction, and ^{133}Cs MAS NMR, in conjunction as previous studies have used X-ray powder diffraction. Neutron diffraction is an excellent tool in the study of pyrochlore-type materials as the O^{2-} superstructure can easily be seen; in addition the scattering factors for all the elements are sufficiently different that Rietveld refinement is easily possible. MAS NMR is ideal to both confirm and provide new positional information on the location of cations within a structure, as the chemical shift and quadrupolar parameters are sensitive to the local surroundings.

2. Experimental

2.1. Sample preparation

Stoichiometric mixtures of $CsTi_{0.5}W_{1.5}O_6$, $CsTi_{0.25}Zr_{0.25}W_{1.5}O_6$, $CsZr_{0.5}W_{1.5}O_6$ and $CsHf_{0.5}W_{1.5}O_6$ were prepared using $CsCO_3$ (Aldrich, 99.99%), TiO_2 (Alfa, 99.9%), ZrO_2 (Alfa, 99.9%) and HfO_2 (Alfa, 99%). TiO_2, ZrO_2, and HfO_2 were prefired at 1123 K for 24 h and then cooled under vacuum to remove CO_2 and H_2O contamination. The oxide powders were ground together in a ball-mill with acetone as solvent. Once ground, the resultant mixtures were dried and pressed into pellets prior to firing. The $CsTi_{0.5}W_{1.5}O_6$ sample was heated at 1123 K for 96 h at a heating rate of 5 K min^{-1}. $CsTi_{0.25}Zr_{0.25}W_{1.5}O_6$, $CsZr_{0.5}W_{1.5}O_6$ and $CsHf_{0.5}W_{1.5}O_6$ were heated at 1173 K for 96 h using an initial heating rate of 5 K min^{-1}. Once cooled the samples were ground in a mortar and pestle to a powder sufficient to easily pass through a 38 μm filter.

2.2. Neutron diffraction

Constant wavelength neutron diffraction patterns were collected, at room temperature, for all samples using the C2-DualSpec diffractometer at the Chalk River National Laboratory, Canada, operating at an incident wavelength of 1.3300 Å (determined using an Al_2O_3 standard). Sample diffraction patterns were collected over the angular range 5–80° 2θ, with an angular resolution of 0.1°, corresponding to a *d*-spacing range of 1.035–15.26 Å.

In classical pyrochlores the use of portions of the pattern to determine such values as unit-cell size, and the 48*f*-positional parameters is well understood and mathematically ideal [10,11]. Such a technique is based on the

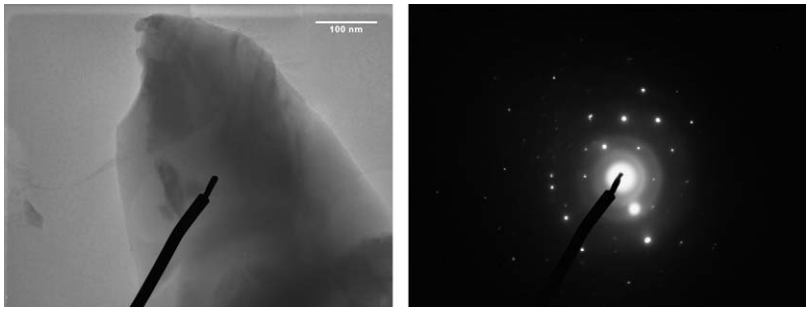

Fig. 2. Bright field image and diffraction pattern for $CsTi_{0.5}W_{1.5}O_6$. Scale bar indicates 100 nm.

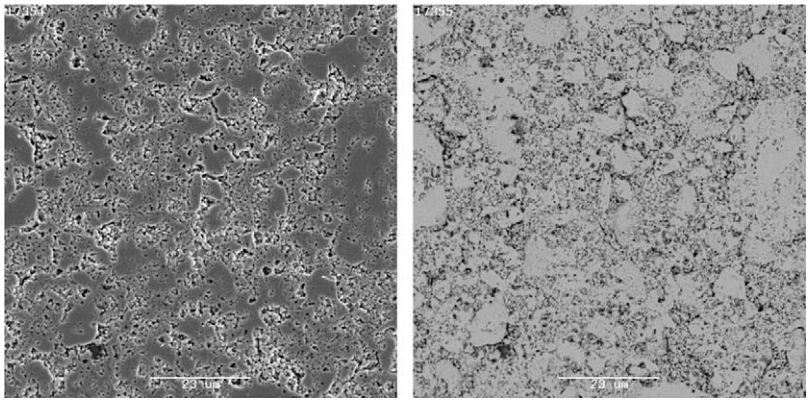

Fig. 3. SEM images from $CsTi_{0.25}Zr_{0.25}W_{1.5}O_6$. The left image is secondary electron, right image is back scattered electron image and the scale bar is 23 μm.

observation that some peaks have entirely cation or anion contribution, and as such allow the values to be determined without reference to other refinable parameters, e.g. the overall scale of the pattern can be found independently of the 48*f*-positional parameter, thus minimising poor refinement. In the defect pyrochlores studied here this technique is not possible. In these pyrochlores the additional 32*e* position complicates the powder diffraction patterns due its contribution to the structure factor. Unlike the classical pyrochlores this position has no conditions limiting the observed reflections in diffraction and as such it contributes to every observed peak from the other sites, 48*f*, and 16*d*. This results in an inability to determine the overall scale factor for the pattern, which in turn prevents both the 32*e* and 48*f* positional parameters being found uniquely. Thus the data were refined using all the peaks available during refinement, with the only constraints being that the *B*-site cations resided on the 16*d* site randomly, and the 32*e* position had a fractional occupancy of 0.25.

The data were analysed by Rietveld refinement using GSAS [12] with the EXPGUI toolkit [13]. The set of instrumental and structural parameters refined were the overall scale factor, unit cell dimensions, a Chebyschev polynomial background function, the widths of the Gaussian and Lorenztian components of a Voigt function describing the reflection line shape, determined using a Le–Bail fit, and the O 48*f*–*x*/Cs 32*e* positional parameters.

2.3. Nuclear magnetic resonance

^{133}Cs $\left(I=\frac{7}{2}\right)$ NMR spectra were acquired using a Chemagnetics Infinity spectrometer, equipped with a 9.4 T magnet and operating at a Larmor frequency (v_0) of 52.5 MHz for ^{133}Cs. Samples were packed into 4-mm diameter ZrO_2 rotors and rotated at a speed of ~12.5 kHz. Spectra were referenced to 1 M CsCl (aq) via a secondary reference of CsCl (s) at 223.3 ppm [14].

Table 1
Results from analytical electron microscope chemical analysis

Composition	Element	Grain 1	Grain 2	Grain 3	Grain 4	Average	Std.dev.
$CsTi_{0.5}W_{1.5}O_6$	W	1.496	1.525	1.479	1.484	1.496	0.020
	Ti	0.492	0.456	0.502	0.500	0.487	0.021
	Zr	0.000	0.000	0.000	0.000	0.000	0.000
	Hf	0.000	0.000	0.000	0.000	0.000	0.000
	Fe	0.012	0.020	0.019	0.015	0.017	0.003
	Cs	0.917	1.045	1.002	1.050	1.003	0.062
$CsHf_{0.4}W_{1.6}O_6$	W	1.585	1.671	1.588		1.615	0.049
	Ti	0.000	0.000	0.000		0.000	0.000
	Zr	0.012	0.011	0.022		0.015	0.006
	Hf	0.384	0.296	0.367		0.349	0.047
	Fe	0.019	0.022	0.023		0.021	0.002
	Cs	1.071	1.122	1.072		1.088	0.029
$CsZr_{0.4}W_{1.6}O_6$	W	1.606	1.626	1.584		1.605	0.021
	Ti	0.013	0.000	0.000		0.004	0.007
	Zr	0.363	0.359	0.400		0.374	0.022
	Hf	0.000	0.000	0.000		0.000	0.000
	Fe	0.018	0.015	0.016		0.016	0.001
	Cs	1.087	1.033	1.099		1.073	0.035

The inclusion of Fe is due to possible contamination from the method of sample preparation.

Table 2
Results from scanning electron microscope—energy-dispersive X-ray characterisation

Composition	Element	Grain 1	Grain 2	Grain 3	Average	Std.dev.
$CsTi_{0.25}Zr_{0.25}W_{1.5}O_6$	W	1.487	1.477	1.492	1.485	0.008
	Ti	0.246	0.290	0.238	0.258	0.028
	Zr	0.249	0.233	0.259	0.247	0.013
	Hf	0.000	0.000	0.005	0.002	0.003
	Fe	0.017	0.000	0.007	0.008	0.009
	Ca	0.007	0.003	0.000	0.003	0.003
	Cs	1.133	1.100	1.089	1.108	0.023

The inclusion of Fe is due to possible contamination from the method of sample preparation.

Table 3
Results from Rietveld refinements where wRp and Rp are those values quoted by GSAS

Element	Wykoff	x	y	z	U_{iso}	Frac
System	$CsTi_{0.5}W_{1.5}O_6$		$a = 10.2763(4)$ Å wRp = 0.0405		vol = 1085.20(7) Å^3 Rp = 0.0276	
Cs	32*e*	0.117(7)	0.117(7)	0.117(7)	0.017(12)	0.25
Ti	16*d*	0.5	0.5	0.5	0.0225(23)	0.25
W	16*d*	0.5	0.5	0.5	0.0225(23)	0.75
O	48*f*	0.43829(15)	0.125	0.125	0.014(9)	1.0
System	$CsTi_{0.25}Zr_{0.25}W_{1.5}O_6$		$a = 10.3403(8)$ Å wRp = 0.0471		vol = 1105.61(15) Å^3 Rp = 0.0358	
Cs	32*e*	0.118(11)	0.118(11)	0.118(11)	0.018(17)	0.25
Ti	16*d*	0.5	0.5	0.5	0.0323(19)	0.125
Zr	16*d*	0.5	0.5	0.5	0.0323(19)	0.125
W	16*d*	0.5	0.5	0.5	0.0323(19)	0.75
O	48*f*	0.43804(19)	0.125	0.125	0.0158(4)	1.0
System	$CsHf_{0.4}W_{1.6}O_6$		$a = 10.3653(14)$ Å wRp = 0.0691		vol = 1113.64(25) Å^3 Rp = 0.0521	
Cs	32*e*	0.1185(20)	0.1185(20)	0.1185(20)	0.07(33)	0.25
Hf	16*d*	0.5	0.5	0.5	0.0313(25)	0.25
W	16*d*	0.5	0.5	0.5	0.0313(25)	0.75
O	48*f*	0.4372(4)	0.125	0.125	0.0145(7)	1.0
System	$CsZr_{0.4}W_{1.6}O_6$		$a = 10.3820(7)$ Å wRp = 0.0487		vol = 1119.03(13) Å^3 Rp = 0.0362	
Cs	32*e*	0.119(7)	0.119(7)	0.119(7)	0.014(14)	0.25
Zr	16*d*	0.5	0.5	0.5	0.0345(19)	0.25
W	16*d*	0.5	0.5	0.5	0.0345(19)	0.75
O	48*f*	0.43760(23)	0.125	0.125	0.0208(9)	1.0

Compositions determined by AEM/SEM and shown in Tables 2 and 3.

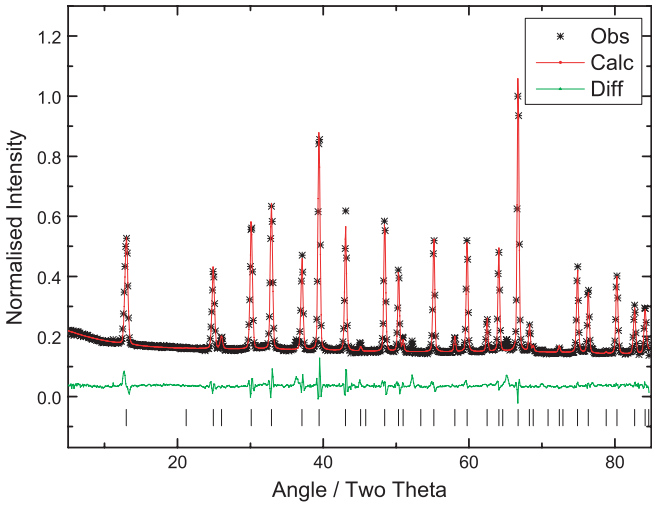

Fig. 4. Example plot of refined model and raw data for $CsTi_{0.5}W_{1.5}O_6$ using GSAS/EXPGUI. Recorded data are shown as points, the refined model is the upper solid line and the difference is the lower solid line. The reflections are marked with the dashes. The peaks at ~37°, 54° and 65° are from an unknown phase not seen in the SEM and not used in the models refined here. These extra peaks were present in all phases.

Typically, pulse durations of ~2.5 μs were employed with a radio frequency field strength of 80 kHz and a recycle interval of 10 s.

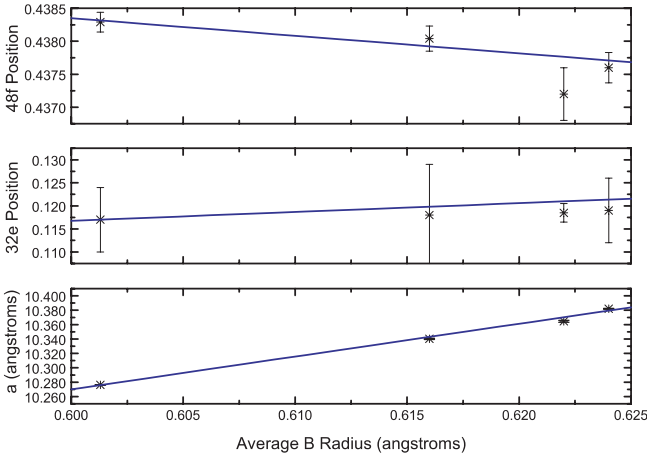

Fig. 5. Plots of unit cell size, 32*e* position (*x*,*x*,*x*), and 48*f* position (*x*,0.125,0.125) as a function of average *B*-site ionic radius. Error bars shown are those given by GSAS.

2.4. Electron microscopy analysis

2.4.1. Analytical electron microscopy

Samples based on the composition $CsTi_{0.5}W_{1.5}O_6$, $CsZr_{0.5}W_{1.5}O_6$ and $CsHf_{0.5}W_{1.5}O_6$ were analysed using TEM/EDX. TEM samples were prepared by crushing

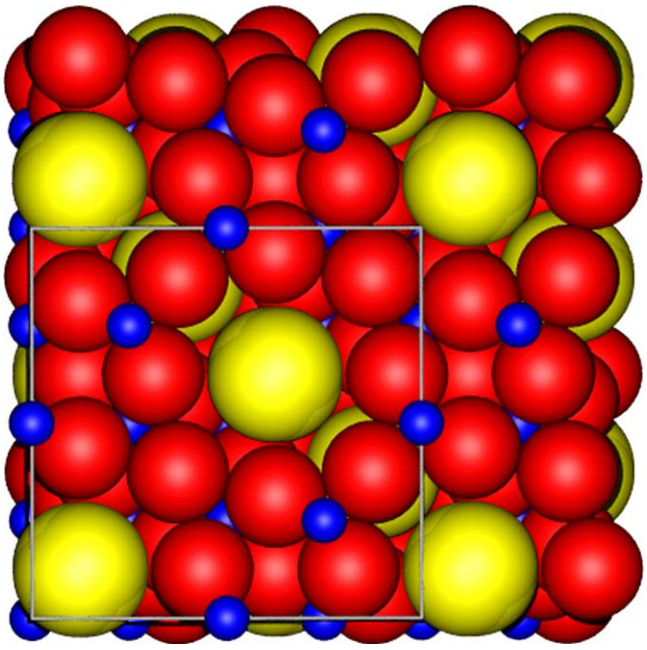

Fig. 6. Unit cell representation of $CsTi_{0.5}W_{1.5}O_6$, projection of the [110] plane. Yellow spheres are Cs^+, red spheres are O^{2-} and blue spheres are the *B*-site. Radii used in this image are from Shannon [6,7].

small fragments in methanol and collecting the suspension on holey carbon-coated copper grids. Samples were using a JEOL 2000FXII TEM operated at 200 kV and calibrated for selected area diffraction over a range of objective lens currents using a gold film standard. The compositions of the grains were checked by EDX analysis using a Link ISIS energy-dispersive spectrometer (EDX) attached to the TEM. The *k*-factors required for the quantitative thin film analyses were determined from a range of synthetic and natural standard materials. Spectra were usually acquired for 600 s and processed using a digital top hat filter to suppress the background, a library of reference spectra for multiple least-squares peak fitting, and a Cliff–Lorimer ratio procedure to reduce the data to weight percent oxides (details are given in Lumpkin et al. [15]). An example bright field image and diffraction pattern is shown in Fig. 2.

2.4.2. Scanning electron microscopy

$CsTi_{0.25}Zr_{0.25}W_{1.5}O_6$ was checked for purity using a JEOL 6400 SEM operating at 15 kV. Microanalyses were obtained using a Noran Voyager EDX attached to this microscope. The instrument was operated in standardless

Table 4
Bond lengths for the first co-ordination sphere of Cs pyrochlores

Composition	Average R_B (Å)	Bond	Length (Å)	Error (Å)	CN
$CsTi_{0.5}W_{1.5}O_6$	0.601	Cs–O	3.14	0.07	3
			3.30	0.07	3
			3.57	0.11	3
			3.719	0.017	6
			3.79	0.09	3
		Ti/W–O	1.9241	0.0005	6
$CsTi_{0.25}Zr_{0.25}W_{1.5}O_6$	0.616	Cs–O	3.16	0.11	3
			3.31	0.12	3
			3.62	0.13	3
			3.702	0.01	6
			3.83	0.18	3
		Ti/Zr/W–O	1.9369	0.0006	6
$CsHf_{0.4}W_{1.6}O_6$	0.622	Cs–O	3.20	0.05	3
			3.27	0.05	3
			3.67	0.07	3
			3.726	0.009	6
			3.76	0.06	3
		Hf/W–O	1.9449	0.0011	6
$CsZr_{0.4}W_{1.6}O_6$	0.624	Cs–O	3.19	0.07	3
			3.31	0.08	3
			3.66	0.09	3
			3.719	0.009	6
			3.82	0.12	3
		Zr/W–O	1.9463	0.008	6

Bond lengths are calculated using refined neutron data and errors are presented in Angstroms, and ionic radii are from Shannon [6,7].

Table 5
Previously published data by Castro et al. [8] for the structure of pyrochlores containing Cs–W and Ti/Hf/Zr.

Composition	Average R_B (Å)	Unit cell–a (Å)	Volume (Å)	32e	48f
$CsTi_{0.5}W_{1.5}O_6$	0.601	10.2710(3)	1083.52(7)	0.112	0.435
$CsHf_{0.5}W_{1.5}O_6$	0.6275	10.3906(3)	1128.4(2)	0.108	0.437
$CsZr_{0.5}W_{1.5}O_6$	0.630	10.4109(5)	1121.8(1)	0.110	0.437

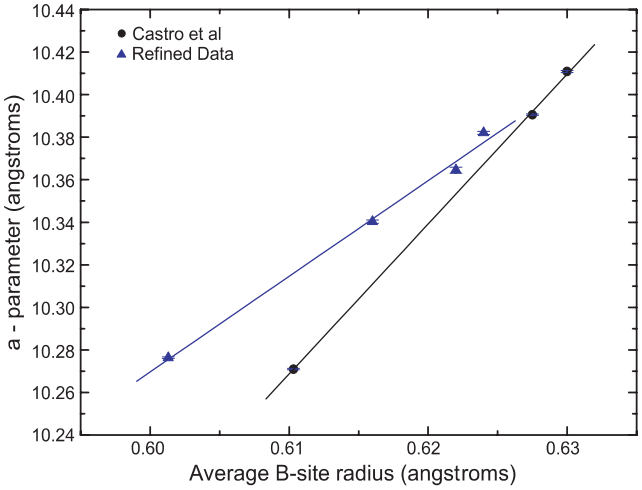

Fig. 7. Plots of refined data and data previously published by Castro et al. [8] as a function of average *B*-site ionic radius. Both data sets have had a linear line fitted to them as a guide.

mode; however, the sensitivity factors were calibrated for semi-quantitative analysis using a range of synthetic and natural standard materials. Spectra were usually acquired for 500 s and reduced to weight percent oxides using a digital top-hat filter to suppress the background, a library of reference spectra for multiple least-squares peak fitting and full matrix (ZAF) corrections.

3. Results and discussion

3.1. Compositional analysis

The samples when viewed by electron microscopy were found to be on the whole homogeneous, with very small particle sizes. These small sizes are most likely due to the method of sintering used, predominantly the decarbonation of $CsCO_3$ in situ. The decarbonation can often leave small voids in the structure, which are then not removed by sintering. Example SEM images are shown in Fig. 3.

The samples were shown by analysis (results shown in Tables 1 and 2) to be in line with the desired compositions. The minor impurity phases were found to be ZrO_2 and HfO_2 both in the monoclinic form. Such phases arise possibly as a result of slight Cs loss from the mixture during the heating. In the subsequent Rietveld refinements the compositions used were those determined by the compositional analysis. The minor phases were tested in the refinements but were found to be undetectable in the neutron diffraction data.

3.2. Rietveld refinement results

The complete refined results for the unit-cell parameters are shown in Table 3. An example result from the refinement, $CsTi_{0.5}W_{1.5}O_6$, is shown pictorially in Fig. 4. When analysing the systems where there is a second phase such as ZrO_2 the extra W is assumed to have partially reduced from W^{6+} to W^{5+}, and such an assumption is valid as CsW_2O_6 is known to exist [16].

The unit-cell parameter a, and subsequently volume, show a linear relationship with the average ionic-size for the *B*-cation, i.e. the larger the average size the larger the unit-cell. This is to be expected, and agrees with Vegard's law, as the only parameter changed is the composition of the *B*-site which in turn will have an effect on the average ionic-radius of the *B*-site, and thus the unit-cell size. A plot showing this is given in Fig. 5, with a linear fit indicated. The results agree with those for classical pyrochlores [4] which show that the unit-cell size is directly related to the average ionic radius of its constituents. A crystallographic representation of the unit-cell is shown in Fig. 6.

The parameters for the 32e and 48f positions additionally show a linear link; the 32e position shows that as the average *B*-site radius increases the *A*-cations move towards the 8a position of $(\frac{1}{8},\frac{1}{8},\frac{1}{8})$. The 48$f$ positional parameter moves back to the 0.4375 thought to be ideal in pyrochlore as the average *B*-site radius increases the 48f position; both observations are shown in Fig. 5. It should be added here that the Hf containing sample lies off the linear line, probably due to some slight sample inconsistencies likely to be in composition, that were not visible in the electron microanalysis.

Across the whole series the local co-ordination is observed to remain constant, with the average Cs–O co-ordination being 6 at ~3.20 Å, and 12 at ~3.70 Å. The *B*-site co-ordination is 6 at ~1.9–1.95 Å. However, it should be noted that although the co-ordination sphere does not change the bond lengths do, the smallest Cs–O bond being in the $CsTi_{0.5}W_{1.5}O_6$, 3.220 Å, while the largest is in $CsZr_{0.4}W_{1.6}O_6$, 3.250 Å. The tabulated values are shown in Table 4.

While the results here are in broad agreement when compared with those previously published [8], shown in

Table 6
Results from bond valence analysis using Eq. (1)

Composition	Average R_B (Å)	Bond	Average length (Å)	CN	Bond valence	Error
$CsTi_{0.5}W_{1.5}O_6$	0.601	Cs–O	3.220	6	1.09	0.201
			3.700	12		
		Ti/W–O	1.924	6	5.58	0.008
$CsTi_{0.25}Zr_{0.25}W_{1.5}O_6$	0.616	Cs–O	3.235	6	1.05	0.294
			3.714	12		
		Ti/Zr/W–O	1.937	6	5.60	0.009
$CsHf_{0.4}W_{1.6}O_6$	0.622	Cs–O	3.235	6	1.02	0.127
			3.721	12		
		Hf/W–O	1.945	6	5.63	0.017
$CsZr_{0.4}W_{1.6}O_6$	0.624	Cs–O	3.250	6	1.00	0.183
			3.730	12		
		Zr/W–O	1.946	6	5.65	0.122

Values for R_0 used in calculation taken from Brese and O'Keefe [17].

Table 5 and compared pictorially in Fig. 7, there is, however a discrepancy. Such a discrepancy is probably due to method of analysis used. In the previous study by Castro et al., a coupled 32*e* and 48*f* positional analysis was carried out. This method varied the 32*e* and 48*f* positions and computed their intensities, using values for Debye–Waller factors based on atomic masses. Once computed these values were compared with measured X-ray diffraction data and the values that gave the lowest difference were chosen. Such a technique is not without its advantages, e.g. it is sometimes easier to see a change in cation ordering; however, X-rays are not very sensitive to O^{2-}. Secondly, an assumption was used that may not be entirely valid, concerning the 48*f* positional parameter. In the previous analysis it was limited to be between 0.420 and 0.438, whereas in the work presented here it was deliberately unconstrained. The use of an unconstrained 48*f* position is based on the observation that in classical pyrochlore one of the limiting factors in the position of the 48*f* oxygen is due to the relaxation into a void which has on the other side an O^{2-}. In these systems there is no adjacent non-48*f* O^{2-}, it is here the much larger Cs^+ cation resides, so the classical limit of 0.4375 is no longer valid.

As the majority of observed diffraction peaks have contributions from both the 32*e* and 48*f* positions any assumption over position can have a drastic effect on the position obtained for the other site, e.g. if the 48*f* position was limited to (0.4375, 0.125, 0.125) then it would have direct implications on the value of 32*e* obtained. Such an effect is minimised by allowing them both to be refined together. Since the intensity contributions of each reflection is different a least-squares refinement technique has many data points to refine with.

Within the recorded patterns there were extra peaks present which were not possible to identify as the intensities were low. In addition to this there were no extra phases visible in the electron microanalysis which could be used as a basis for identification.

3.3. Bond valence summations (BVS)

BVS is routinely used for analysing bond lengths in structures to help confirm the accuracy of the refined result. Using the previously published equation by Brown and Orlov et al. the values for S_{ij} was calculated and tabulated in Table 6. A plot of S_{ij} against average *B*-site radius is shown in Fig. 8.

The average BVS for the *A*-site tends to decrease to about 1 as the *B*-site radius increases. However, since the change in values is 0.09 and the average error on the measurements is 0.2 this can be thought of as remaining constant. The change in calculated *B*-site can also be thought of as remaining constant not only due to the errors in BVS analysis, but also due to the lack of reliable data on the bond lengths in W^{5+} oxides. Since the BVS is based upon the use of empirical values which are then used to calculate a distance or charge, the effect of a mixed valance cation can be accounted for, using a summation of the various standard values. However, in the case of W^{5+} such values do not exist so could not be used. It is likely that if W^{5+} standard values could be included the BVS for the *B*-site would reduce, close to an expected value of 5.5, for those phases where there is W^{5+} present, e.g. $CsZr_{0.4}W_{1.6}O_6$.

3.4. ^{133}Cs MAS NMR

The ^{133}Cs MAS NMR spectra exhibit single symmetrical resonances, as shown in Fig. 9. The chemical shift (δ) changes linearly as the composition is changed, as shown in Fig. 10 and Table 7. However, rather than the link being with the average ionic-radius of the *B*-site, it is with the electronegativity of the non-W cations, i.e. Ti, Ti/Zr, Hf and Zr. Such a change is understandable as within the structure the Cs is sufficiently close to the *B*-site to be affected by any change in the composition of this site.

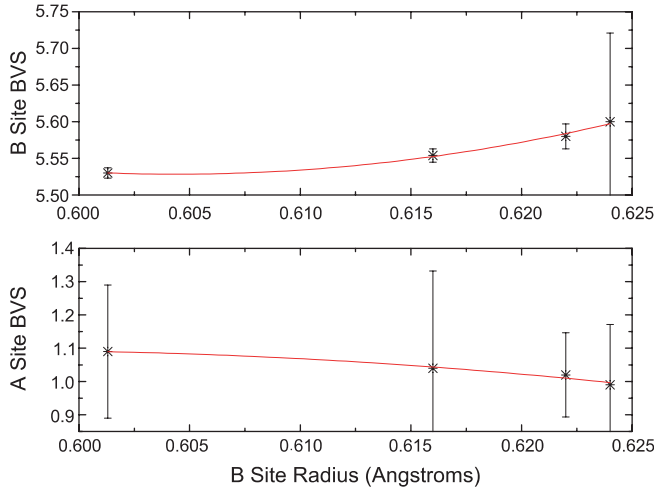

Fig. 8. Plots of bond valence sum (BVS) against average *B*-site ionic radius, lines fitted as a guide to show slight deviation of calculated values.

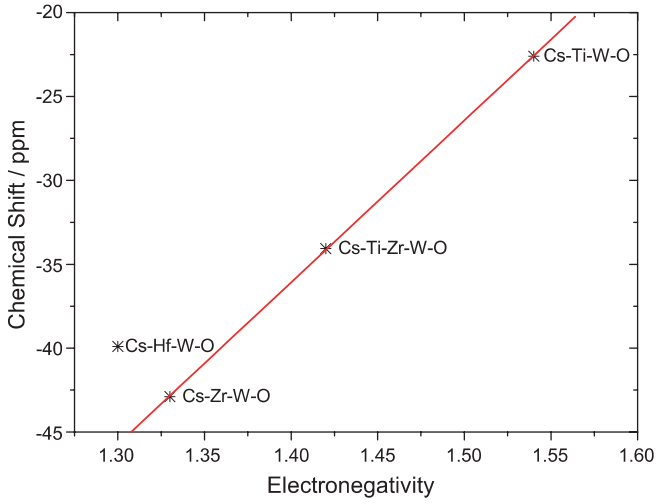

Fig. 10. ^{133}Cs chemical shift shown as a function of the Pauling electronegativity of the changed *B*-site cation; linear line fitted as a guide.

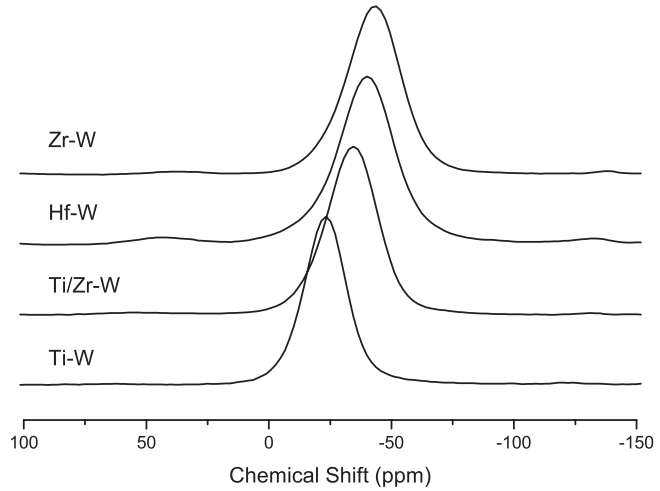

Fig. 9. ^{133}Cs (52.5 MHz) MAS NMR spectra of $CsTi_{0.5}W_{1.5}O_6$, $CsTi_{0.25}Zr_{0.25}W_{1.5}O_6$, $CsHf_{0.4}W_{1.6}O_6$ and $CsZr_{0.4}W_{1.6}O_6$, referenced to 1 M CsCl (aq). Spectra show one broad symmetrical peak indicative of a single disordered Cs site in the lattice.

There was no evidence for any preferred ordering in the position of the Cs within the unit-cell. If ordering was present it would be expected to show up either as a peak asymmetry or as distinct resonances within the spectrum. There is however, evidence for disorder in the Cs environment, in the width of resonances observed, such an observation agrees with the postulation that the 32*e* only allows a 0.25 fractional occupancy, but there are four possible, very closely related, positions for it to occupy.

The MAS NMR results agree with the electron micro-analysis showing the presence of 1 cesium-containing phase. The changes in chemical shift reflect the local electron density and thus a correlation with the *B*-site electronegativity. This agrees with the neutron diffraction analysis, i.e. the MAS NMR shows the Cs locating on a disordered 32*e* site, when the *B*-site cations are being changed. The MAS NMR therefore acts as a means of validating the results.

Table 7
Chemical shift and linewidth (full-width half-maximum) of resonances in the ^{133}Cs MAS NMR spectra

Composition	Chemical shift (ppm)	FWHM (Hz)
$CsTi_{0.5}W_{1.5}O_6$	−22.6	978
$CsTi_{0.25}Zr_{0.25}W_{1.5}O_6$	−34.06	1111
$CsHf_{0.4}W_{1.6}O_6$	−39.9	1184
$CsZr_{0.4}W_{1.6}O_6$	−42.9	1274

Chemical shifts are referenced to 1 M CsCl (aq).

4. Conclusion

The pyrochlore systems studied here have been shown to have their unit-cell parameters linked linearly to their average *B*-site radius. The relaxation of the 48*f* oxygen position is directly related to the position of the Cs^+ as it is itself linked to the average *B*-site radius. The ^{133}Cs MAS NMR parameters have been shown to be linked to the electronegativity of the non-W *B*-site cation, and also indicating that there is only one Cs site with positional disorder. This agrees with the postulation that the 32*e* position is disordered with partial occupancy.

Acknowledgments

The authors wish to acknowledge the facilities provided by the Chalk River nuclear laboratories and the help provided by Dr. L.M.D. Cranswick and Dr. I.P. Swainson. The authors (KRW) wish to acknowledge the Cambridge-MIT Institute (CMI) for funding this work. The provision of a Royal Society Dorothy Hodgkin research fellowship is also acknowledged (SEA).

References

[1] H. Yamamura, H. Nishino, K. Kakinuma, K. Nomura, Solid State Ionics 158 (2003) 359.
[2] S.L. Chamberlain, S.T. Hess, L.R. Corruccini, Phys. Lett. A 323 (2004) 310.
[3] S.V. Yudintsev, Geol. Ore Deposits 45 (2003) 151.
[4] B.C. Chakoumakos, J. Solid State Chem. 53 (1984) 120.
[5] M.A. Subramanian, G. Aravamudan, G.V.S. Rao, Prog. Solid State Chem. 15 (1983) 55.
[6] R.D. Shannon, Acta Crystallogr. Section A A32 (1976) 751.
[7] R.D. Shannon, C.T. Prewitt, Acta Crystallogr. Section B—Struct. Sci. B 25 (1969) 925.
[8] A. Castro, I. Rasines, X.M. Turillas, J. Solid State Chem. 80 (1989) 227.
[9] J. Lian, J. Chen, L.M. Wang, R.C. Ewing, J.M. Farmer, L.A. Boatner, K.B. Helean, Phys. Rev. B 68 (2003) 134107.
[10] K.W. Eberman, B.J. Wuensch, J.D. Jorgensen, Solid State Ionics 148 (2002) 521.
[11] C. Heremans, B.J. Wuensch, J.K. Stalick, E. Prince, J. Solid State Chem. 117 (1995) 108.
[12] A.C. Larson, R.B. Von Dreele, General Structure Analysis System (GSAS), Los Alamos National Laboratory Report LAUR, 2000.
[13] B.H. Toby, J. Appl. Crystallogr. 34 (2001) 210.
[14] S. Mooibroek, R.E. Wasylishen, R. Dickson, G. Facey, B.A. Pettitt, J. Magn. Reson. 66 (1986) 542.
[15] G.R. Lumpkin, K.L. Smith, M.G. Blackford, R. Giere, C.T. Williams, Micron 25 (1994) 581.
[16] R.J.R. Cava, T. Siegrist, B. Hessen, J.J. Krajewski, W.F. Peck Jr., J. Solid State Chem. 103 (1993) 359.
[17] N.E. Brese, M. O'Keeffe, Acta Crystallogr. Section B—Struct. Sci. B 47 (1991) 192.